Energy Conversion and Management 306 (2024) 118308

Contents lists available at ScienceDirect

Energy Conversion and Management

journal homepage: www.elsevier.com/locate/enconman

Research Paper

A hydrogen-fuelled compressed air energy storage system for flexibility reinforcement and variable renewable energy integration in grids with high generation curtailment

Luca Migliari *, Davide Micheletto, Daniele Cocco

Department of Mechanical, Chemical and Materials Engineering, University of Cagliari, Via Marengo, 2 09123 Cagliari, Italy

ARTICLE INFO

Keywords:
Photovoltaic
Hydrogen
Grid security
RES
Ancillary service
CAES

ABSTRACT

Globally, the increasing share of renewables, prominently driven by intermittent sources such as solar and wind power, poses significant challenges to the reliability of current electrical infrastructures, leading to the adoption of extreme measures such as generation curtailment to preserve grid security. Within this framework, it is essential to develop energy storage systems that contribute to reinforce the flexibility and security of power grids while simultaneously reducing the share of generation curtailment. Therefore, this study investigates the performance of an integrated photovoltaic-hydrogen fuelled-compressed air energy storage system, whose configuration is specifically conceived to enable the connection of additional intermittent sources in already saturated grids. The yearly and seasonal performance of the integrated energy storage system, specifically designed to supply flexibility services, are evaluated for a scenario represented by a real grid with high-variable renewables penetration and frequent dispatchability issues. Results show that the integrated system, with performance-optimized components and a new energy management strategy, minimizes photovoltaic energy curtailment, otherwise around 50%, to as low as 4% per year, achieving system efficiencies of up to 62%, and reinforces the grid by supplying inertial power for up to 20% of nighttime hours. In conclusion, the integrated plant, operating with zero emissions, on-site hydrogen production, and optimized for non-dispatchable photovoltaic energy utilization, proves to be effective in integrating new variable renewable sources and reinforcing saturated grids, particularly during spring and summer.

1. Introduction

The global production of Renewable Energy Sources (RES) exceeded 7,857 TWh in 2021, with an installed capacity of 3,381 GW, of which more than 57 % was from variable Renewable Energy Sources (VRES) (898 GW from wind turbines and 1,055 GW from photovoltaic plants). According to the International Energy Agency (IEA) [1], the planned global renewable capacity additions were expected to reach more than 440 GW in 2023, about 290 GW from solar energy and 107 GW from wind energy. This increasing share of VRES poses significant challenges to the electric grids: in many countries with VRES share above 20 % and limited synchronous interconnections with neighboring states, the lack of grid flexibility requires frequent generation curtailment and load shedding to maintain grid security [1]. For example, California's yearly photovoltaic (PV) curtailments, which reached 22 % in April 2023, almost doubled in the last five years, rising from 3.2 % in 2019 up to 6.2 % in 2022 [2]. Apart from the environmental detriment, RES generation curtailment entails other adverse effects: in fact, it reduces RES economic convenience and attractiveness [3]. For these reasons, several authors, including López et al. [4], stated that, in regions like California, the foreseen growth in VRES penetration will increasingly require measures to mitigate generation curtailment and address grid flexibility challenges [5]. Among the useful actions, IEA [6], in agreement with the scientific community, considers as key measures the introduction of Energy Storage Systems (ESS) [7], the deployment of RES power plants able to provide inertia and the growth of demand response services [8]. Apart from Battery Energy Storage Systems (BESS), which are expected to account in Europe for a 20–30 % share of total dispatchable capacity energy by 2050, Thermo Mechanical Energy Storage (TMES) and Hydrogen are among the most promising technologies for decarbonizing energy systems [9], providing flexibility services [10] and improving grid adequacy [11], even for small scale applications [12].

Thanks to their suitability in providing flexibility services,

* Corresponding author.
E-mail address: luca.migliari@unica.it (L. Migliari).

https://doi.org/10.1016/j.enconman.2024.118308
Received 22 January 2024; Received in revised form 11 March 2024; Accepted 12 March 2024
Available online 16 March 2024

Nomenclature

Symbols

c	Specific heat [kJ/kgK]
E	Energy [kWh]
$\dot{E}$	Power [kW]
GI	Global solar irradiance [W/m^2]
γ	Heat capacity ratio [-]
LHV	Lower heating value [MJ/kg]
M	Mass [kg]
$\dot{m}$	Mass flow rate [kg/s]
Q	Thermal energy [kW]
$\dot{Q}$	Thermal power [kW]
R	Gas constant [J/kgK]
t	Time [h]
T	Temperature [°C]
V	Volume [m^3]
η	Efficiency [-]
ρ	Density [kg/m^3]

Subscripts

air	Air
C	Compressor
CC	Combustion Chamber
ch	Charge
dch	Discharge
DH	Dark Hours
g	Burnt gases
H_2	Hydrogen
in	Inlet section
is	Isentropic
out	Outlet section
RT	Round Trip
T	Turbine

Acronyms

CAES	Compressed Air Energy Storage
CF	Capacity Factor
EMS	Energy Management Strategy
EOH	Equivalent Operating Hours
G	Grid
HP	High Pressure
LP	Low Pressure
PEM	Proton Exchange Membrane
PR	Pressure Regulator
PV	Photovoltaic
RES	Renewable Energy Sources
VRES	Variable Renewable Energy Source

Compressed Air Energy Storage (CAES) are TMES systems that have recently regained attention, despite the fact that their technology is not novel: in fact, the McIntosh [13] and Huntorf [14] plants have been operational for over 30 years. CAES systems work by using a compressor to convert electrical energy into compressed air (demand response service), which is stored in a reservoir, natural cavern, or disused mine (energy storage service) and later expanded through a turbine (inertia generation service). Several CAES configurations were proposed and studied in the last years. In the Adiabatic Compressed Air Energy Storage (A-CAES) systems [15], the heat generated during air compression is recovered, stored in a Thermal Energy Storage (TES), and later used to heat the air before expansion, while in the Diabatic configuration (D-CAES) external combustion occurs to heat up the compressed air before expansion. A-CAES systems allow to avoid the use of fossil fuels for the combustion process, but their flexibility service is strongly limited by the restricted operative range of the compression train and by the TES state of charge [16]. Similarly to A-CAES systems, the new hydrogen-powered D-CAES concept avoids the use of fossil fuels but overcomes the flexibility limitations through the introduction of electrolyzers, whose operational range is much broader [17]. Obviously, the Net Zero 2050 scenario, in which the electricity output from unabated methane is foreseen to virtually disappear [18], requires that the hydrogen used by these H_2-powered D-CAES systems comes from RES.

CAES systems recently received both commercial and (especially in the hydrogen-powered version) research interest. Several commercial projects of CAES in different configurations exist worldwide: a 60 MW plant was recently connected to the grid in Jiangsu (China), while a 350 MW plant is currently under construction in Shangdong (China) and other projects are under development in Zuidwending (Netherlands), California (United States) and New South Wales (Australia) [19].

Research interest is primarily focused on energy-environmental assessments, and in some cases, on economic analyses of hybrid or integrated CAES systems. For example, a recent study on an integrated CAES configuration was developed by Assareh and Ghafouri [20], which proposed a cogeneration system (electricity, heating, and cooling) based on CAES, solar, and geothermal energy. The system comprises a solar field (parabolic through collectors), a gas turbine, an absorption chiller, and a CAES. The performance of the plant was optimized for exergy efficiency maximization and cost rate minimization, calculating optimal values of 29.25 % and 714.25 $/h respectively, in 5 regions in Iran considered as case studies. Also, Xue et al. [21] proposed a combined cycle system using an electrolyzer and a CAES system to store energy, to later be released generating electricity using a solid oxide fuel cell, a gas turbine, and a steam turbine: the system can reach an efficiency of 39.45 %. In the field of hybrid solutions, Bartela et al. [22] studied a hybrid CAES system composed of a hydrogen production system, a methanation unit, a CAES, an oxy-combustion section, and a drying system. Another example of system integration is developed by Alirahmi et al. [23] and regards a solar heliostat-driven combined cycle coupled with a regenerative hydrogen-fed D-CAES system, designed for a thermal-integrated application. In this system, excess electricity from the combined plant is used to power the compression train of the CAES, and to produce hydrogen in a Proton Exchange Membrane (PEM) electrolyzer. Thermal energy, which is recovered from the compression train, heats up the water for domestic applications and for the electrolyzer. A similar system, involving a PEM electrolyzer coupled to a CAES, was proposed by Zhao et al. [24], who studied a hydrogen-fuelled D-CAES configuration, composed of a gas turbine thermally integrated with a fuel cell. The system components work in combination to smooth the RES power fluctuations and provide hot water and power to a community. The research interest in coupling hydrogen with CAES systems is confirmed by Cao et al. [25], which proposed a hydrogen-fueled CAES, where excess RES energy is used to drive the air compressors and generate hydrogen. The storage system of this layout comprises a high-pressure air storage reservoir, a hydrogen storage tank, and a two-tank thermal energy storage of water. The system of Cao et al. [25] is characterized by a round trip efficiency of 65.11 % and an exergy efficiency of 79.23 %. The system efficiency could be further improved by means of higher combustion temperatures and more performing electrolyzers. A preliminary study on the performance analysis of a D-CAES system fuelled by green hydrogen in comparison with natural-gas [17] was also conducted by the authors. Among the existing technologies for hydrogen production through water electrolysis, almost all the hydrogen-integrated CAES systems involve PEM electrolyzers [23], even if, as it is well known, other valid technologies exist, including alkaline, Anion Exchange Membrane (AEM) and Solid Oxide Electrolyzer Cell (SOEC)

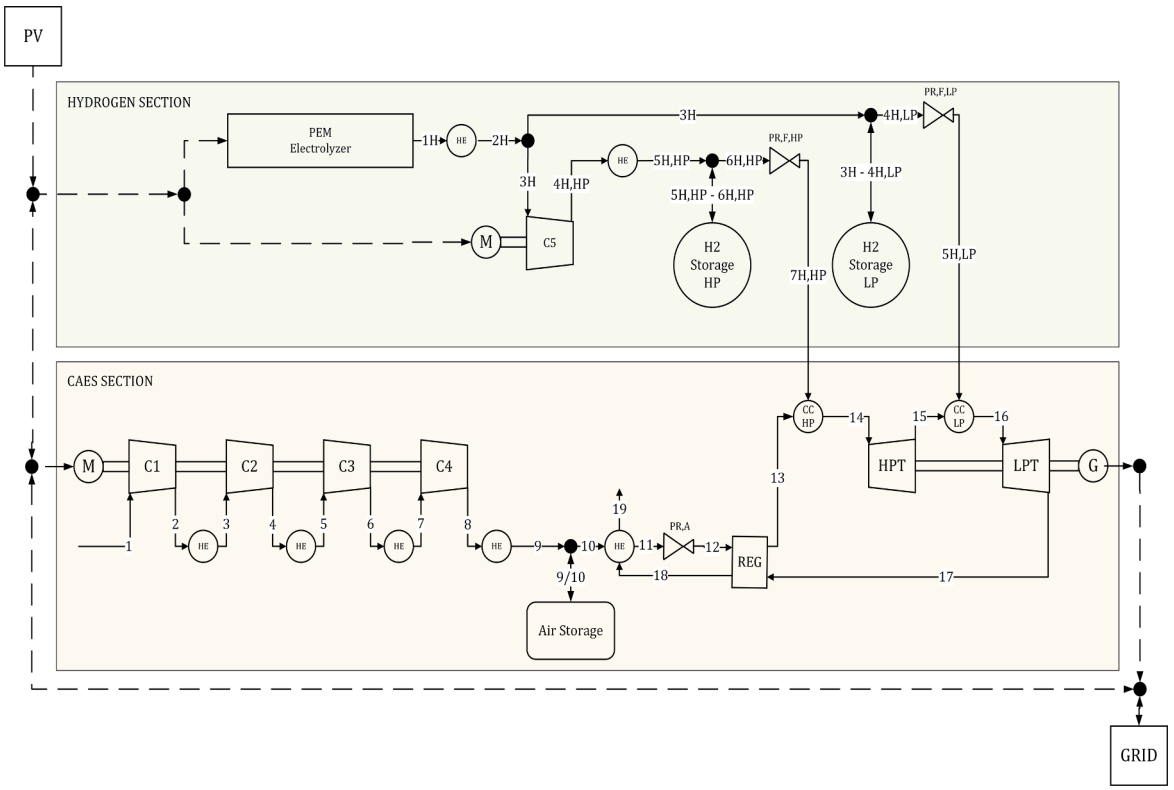

Fig. 1. Schematic configuration of the integrated PV-H_2-CAES system.

[26]. Alkaline electrolyzers are recognized as the most cost-effective solution, being highly efficient and commercially mature. However, they are characterized by a slow response time compared to PEM electrolyzers. AEM electrolyzers perform similarly to PEM electrolyzers, but use potentially low-cost materials; however, their commercial availability is still limited. SOEC electrolyzers operate at higher temperatures [27] and higher efficiencies than PEM electrolyzers, but they have longer start-up and response times [26].

Despite the interest in CAES systems being motivated by their capability to provide flexibility services, to the authors' best knowledge, no study assessed the performance of CAES systems based on the flexibility services they can provide to electrical grids. Furthermore, although several studies investigated the integration of hydrogen in the combustion section, none of them considered the optimization of the size of the hydrogen production and storage sections. In addition, very few studies considered the dynamic performance of the CAES components which mainly operate at off-design conditions, such as the compressor, being this crucial for VRES-powered plants. In this framework, this work aims to contribute to the new body of knowledge in the field of CAES systems through the development of a PV power plant integrated with a hydrogen-fuelled D-CAES (PV-H_2-CAES) system specifically designed to improve the flexibility of the electrical grids. In fact, the integrated PV-H_2-CAES system is designed to mitigate the variability in VRES feed-ins, reduce curtailments, supply inertial power, and help address high ramp rates and ramping ranges in a flexibility service supply which considers dispatch possibility contingent on grid conditions. In particular, differently to most of recent studies on CAES solutions, where all the energy produced is considered fully dispatchable [20] or where the analyses are carried out only at nominal conditions [25], the present study introduces a performance evaluation methodology that considers a real one-year-long grid scenario, characterized by significant and frequent dispatchability issues. Moreover, the study assesses the size of the main plant components by taking into account the dynamic behaviour of the compressor train, in order to maximise the flexibility services and evaluates the yearly and seasonal performance of an optimised configuration. The energy requirements of both the air compression and hydrogen production sections are thoroughly analyzed, under various scenarios assessing the performance of the integrated system, always with the assumption of utilizing the excess energy production of the PV power plant. The results demonstrate that the proposed integrated PV-H_2-CAES plant is able to effectively improve the grid security providing flexibility services with zero carbon dioxide emissions. Furthermore, it is able to produce RES power during dark hours, thus increasing the RES share on baseload generation.

2. Methods

A schematic configuration of the integrated PV-H_2-CAES plant is reported in Fig. 1. It is originated from a down-scaled version of the McIntosh CAES plant, which was already demonstrated to be suited for leveling variable wind power [28], with the key difference that hydrogen replaces natural gas as fuel. The charge components of the CAES section of the plant include four inter-refrigerated multistage centrifugal compressors (C), an aftercooler, and an Air Storage system. The discharge components include a high-pressure turbine (HPT) and a low-pressure turbine (LPT), each with a dedicated combustion chamber (CC). In order to operate the expansion train in a "constant pressure mode" [29] as for the McIntosh CAES plant, the air pressure during discharge is controlled by a pressure regulator (PR). A regenerator (REG) and an additional heat exchanger allow to recover part of the thermal energy of the exhaust gases. A green hydrogen production and storage section is added to the plant layout and is based on a PEM electrolyzer for hydrogen generation, which is stored in two dedicated (HP and LP) hydrogen storage tanks. The Balance of Plant is completed by a hydrogen compressor, dedicated heat exchangers, pressure regulators, and other minor components. In this integrated PV-H_2-CAES plant, the electric power for air compression and hydrogen production comes from a dedicated PV system. However, it is important to note that the flexibility of this integrated configuration also enables it to be powered by other VRES power plants and by the grid, either entirely or partially,

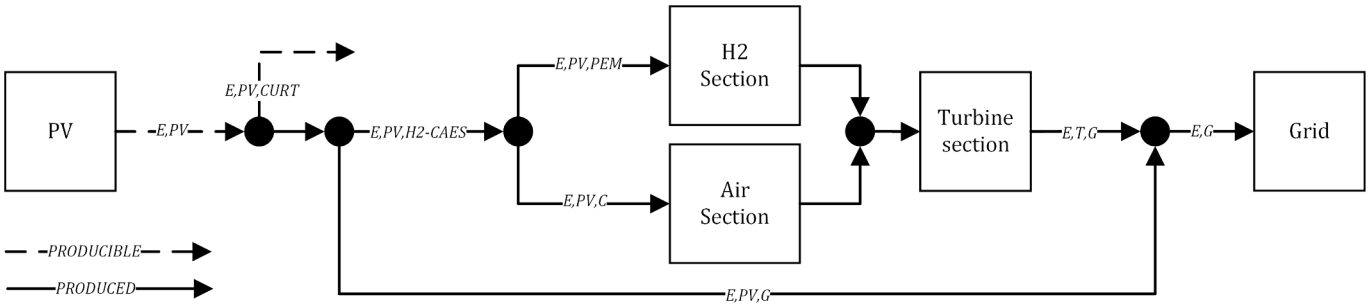

Fig. 2. Main energy flows of the integrated PV-H_2-CAES system.

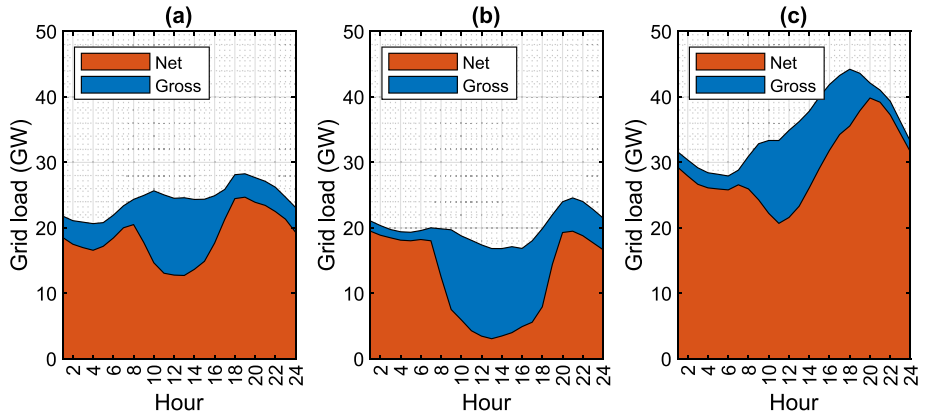

Fig. 3. CAISO duck curves on January 16(a), April 16(b), and August 16(c), 2023.

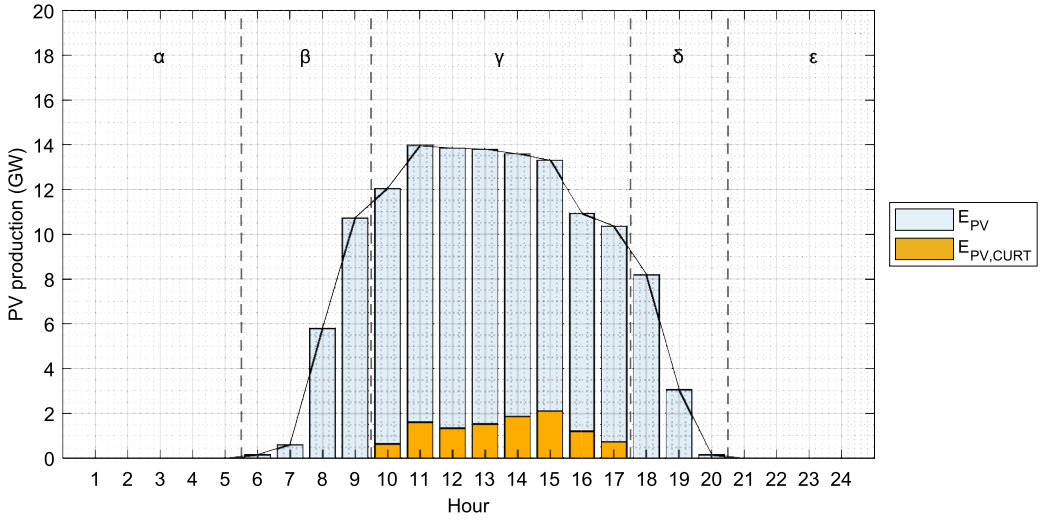

Fig. 4. Daily PV curtailment in the CAISO grid on April 16, 2023.

allowing it to offer demand-response services.

Among the existing technologies for hydrogen production through water electrolysis, a PEM electrolyzer is selected, according to the authors reported in the introduction as well as to Alirahmi et al. [23], because of its wide power range, low operating temperature [27] and rapid response time [26], which make it the most suitable technology for VRES integration.

The main energy flows of the integrated PV-H_2-CAES plant are shown in Fig. 2. In the present paper, E_{PV} represents the energy that could potentially be produced by the PV system without any generation curtailment; therefore, E_{PV} includes a share of energy which is actually generated ($E_{PV,H2-CAES} + E_{PV,G}$) and a share of energy that could potentially be generated if not curtailed ($E_{PV,CURT}$). The energy actually generated by the PV system can be directly fed in the grid ($E_{PV,G}$) or used to charge the CAES system ($E_{PV,H2-CAES}$). When the charge phase occurs, the energy is used for compressing air ($E_{PV,C}$) and producing hydrogen ($E_{PV,PEM}$), which are stored for a later use. During the discharge phase, the stored energy is used to generate electricity ($E_{T,G}$). Therefore, the overall energy delivered to the grid (E_G) is the sum of $E_{PV,G}$ and $E_{T,G}$.

2.1. Energy management strategy

The Energy Management Strategy (EMS) of the integrated PV-H_2-CAES system is conceived to integrate the PV energy production into electrical grids already characterized by a high VRES penetration, where any additional increase in VRES power would result in further

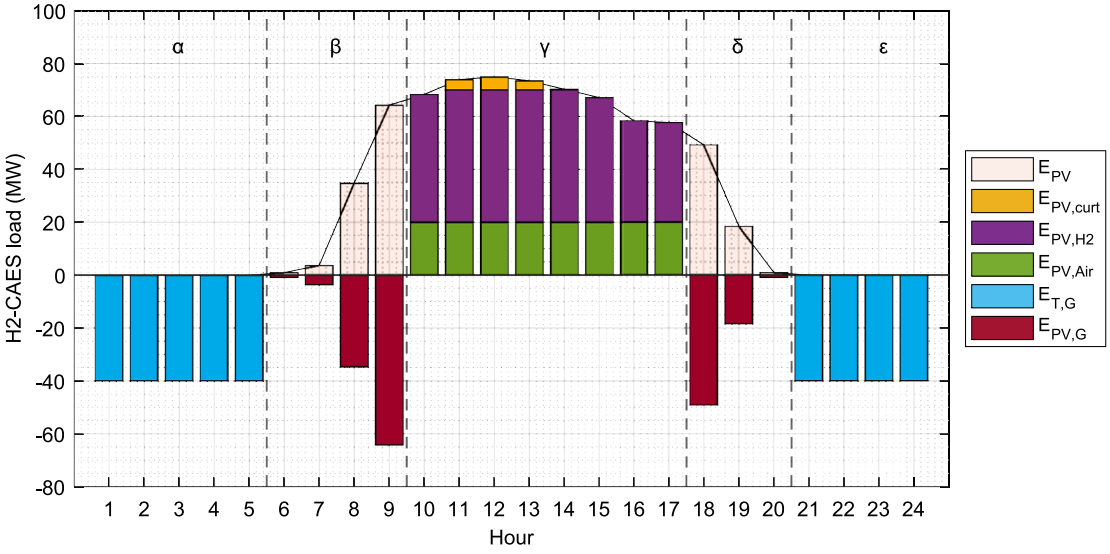

Fig. 5. Energy management strategy of the PV-H_2-CAES system.

deterioration of flexibility levels (uncertainty in production, extended ramping-ranges, high ramp-rates) and, lastly, generation curtailment. Real examples of extended ramping ranges and high ramp rates are given by the so-called "duck curves" reported in Fig. 3(a-c), showing the California Independent System Operator (CAISO) gross and net[1] grid load on the 16 of January, April, and August of 2023 [2].

With reference to the CAISO duck curve on April 16, 2023, Fig. 4 shows the daily PV potential energy production (E_{PV}) and the corresponding energy curtailment ($E_{PV,CURT}$). Five periods can be identified, herein denoted by the letters α to ε, where α and ε represent the dark hours and β, γ, δ the daylight hours, when PV generation occurs. During early morning (β) and late evening (δ) hours, all the generated PV energy is consumed. Conversely, during the central daylight hours (γ), the PV production exceeds the demand to the extent that the surplus energy cannot be traded with neighbouring countries and must be curtailed. The generation curtailment occurs because of the reached minimum limit in the net load curve, which cannot be reduced to zero due to the technical minima and the response times of those power facilities that are crucial for ensuring grid safety. Given this, it is evident that for such a grid it would be desirable to minimize PV curtailment by storing the excess production for a subsequent use. Clearly, new PV installations would lead to an increase in the generation curtailment shares.

Therefore, the EMS proposed for the PV-H_2-CAES system is conceived to enhance the grid flexibility, thus enabling the installation of new PV capacity.

As abovementioned, the PV-H_2-CAES system can directly feed the PV power into the grid or use it for charging the energy storage sections. Clearly, from an efficiency point of view, direct feed-in is the preferable option. However, with reference to the above-mentioned five periods experienced in electrical grids with high shares of VRES plants, the EMS applied to the PV-H_2-CAES plant considers that:

1. during the early morning (β) and late evening (δ) hours the PV power is directly fed to the grid;
2. during the generation curtailment periods (γ), the PV power is used to power both the air compressor and the PEM electrolyzer, prioritizing the air compressor;
3. during dark hours (α and ε), the CAES is discharged.

[1] The net load is given by the difference of the gross load and the electricity generated from VRES (wind and solar).

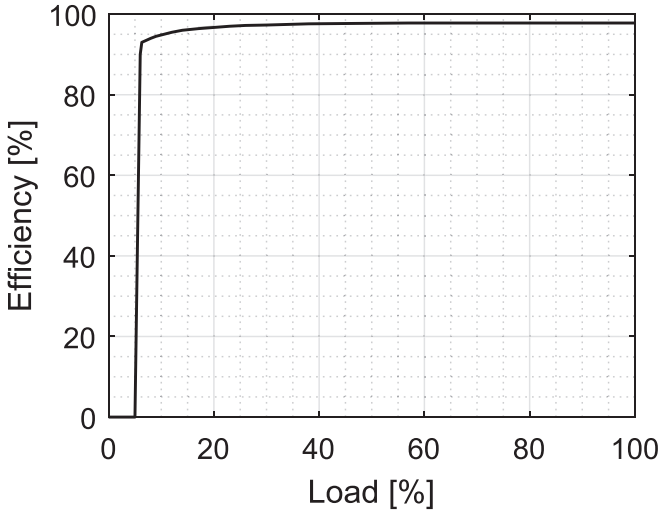

Fig. 6. Inverter efficiency as a function of the load.

The EMS of the PV-H_2-CAES systems is better explained in Fig. 5. During early morning (β) and late evening (δ) hours the considered grid has the capacity to dispatch additional PV power (no curtailments), and therefore the PV power can be directly fed into the grid, resulting in valuable support for ramp rate reduction. Although it is not the case for the EMS applied in this study, in grids without the capacity to dispatch additional VRES power, the PV power can be used to charge the CAES section even during β and δ periods.

During the generation curtailment periods (γ), since any additional PV feed-in would be curtailed, the PV power is used to charge the CAES section. This way, the PV generation is not curtailed, nor does it worsen the flexibility of the grid. More in detail, during the charge phase the PV power is used to power both the air compressor and the PEM electrolyzer. The electrolyzer is powered residually compared to the compressor due to its greater load modulation capability, making it excellent for performing peak shaving of PV plants (smoothing of uncertainty in production). Clearly, in cases of full storage or maximum power capacity of the compressor and electrolyzer, any excess PV power is considered curtailed.

Finally, the discharge of the CAES section during dark hours (α and ε), allows to enhance the share of energy produced during dark hours from RES, providing inertia, and increasing the energy independence of

Table 1
PV system design parameters.

Parameter	Value	Unit
Nominal power of a PV module [34]	360	Wp
Tilt angle	30	°
Azimuth angle	0	°
Derating factor (f_{PV})	0.90	
Nominal inverter efficiency (η_{INV})	0.978	
STC conversion efficiency of a module ($\eta_{PV,STC}$)	0.221	
STC cell temperature (T_{STC})	25	°C
Net Operative Cell Temperature (*NOCT*)	41.5	°C
Ambient temperature at NOCT conditions ($T_{AMB,NOCT}$)	20	°C
Global Solar Irradiation at NOCT conditions (GI_{NOCT})	800	W/m^2
Solar transmittance and absorptance (τ_α)	0.9	
Temperature correction factor (θ)	$-0.29{\cdot}10^{-2}$	1/K

Table 2
PEM electrolyzer design parameters.

Parameter	Value	Unit
Nominal power [36]	2	MW
Transfer coefficient α_{PEM} [35]	0.34	
Constant coefficient β_{PEM} [35]	0.06	
Membrane thickness δ_m [35]	0.04	cm
Humidification factor λ_E [35]	17	
Membrane cross section area *A* [35]	100	cm^2
Faraday constant *F*	96485.33	$\frac{C}{mol}$
Diffusion limit current density i_{lim} [35]	1.55	$\frac{A}{cm^2}$
Exchange current density i_0 [35]	0.0013	$\frac{A}{cm^2}$
Pump and heater energy consumption*	0.3	%
Operating pressure [36]	30	bar
Operating temperature [36]	40	°C
Specific H_2 production	17	$\frac{kg\ h^{-1}}{MW}$

* Referred to total required by the electrolyzer.

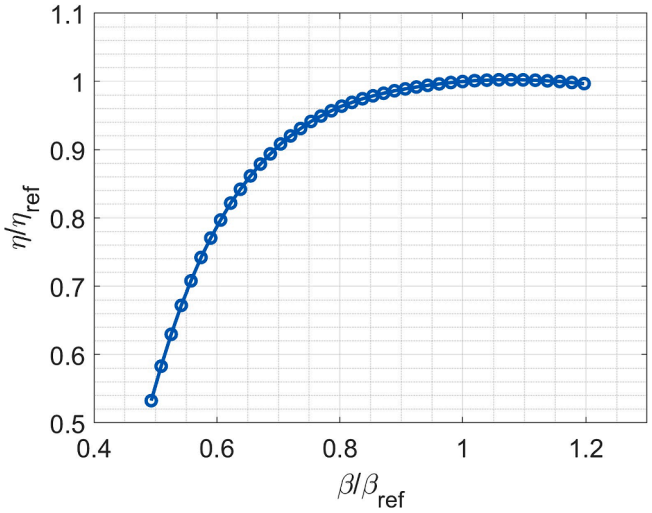

Fig. 7. Compressor generalized efficiency profile.

the grid. However, if the grid were to require additional power during other moments of the day, the flexibility of the system would allow for a discharge phase, operated rapidly thanks to the brief startup time of a conventional gas turbine.

2.2. Mathematical model

The following paragraphs report the mathematical models of each section of the integrated PV-H_2-CAES plant. The models are developed using MATLAB software version R2023a Update 3 [30]. Computational

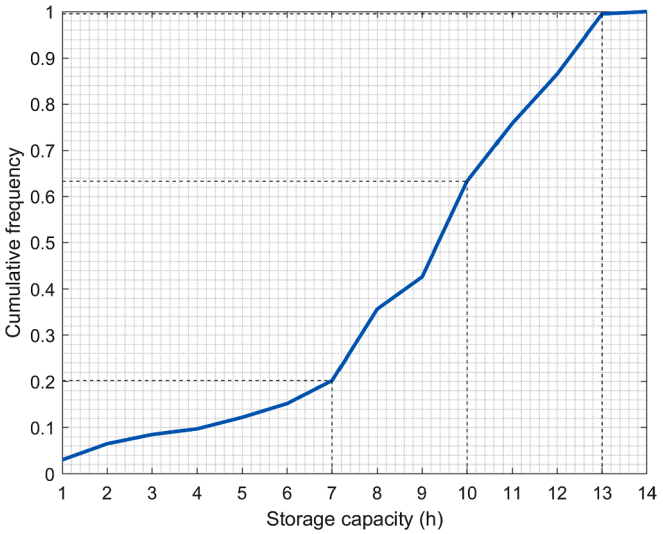

Fig. 8. Cumulative frequency of consecutive dark hours in California in 2022.

Table 3
Integrated PV-H_2-CAES plant design parameters.

Parameter	Value	Unit
Turboexpander power $\dot{E}_T$	42	MW
Photovoltaic power $\dot{E}_{PV}$	$(0.5\ -2){\cdot}\dot{E}_T$	MW
Compressor power $\dot{E}_C$	$(0.1\ -1){\cdot}\dot{E}_{PV}$	MW
Electrolyzer power $\dot{E}_{PEM}$	$(0.1\ -1){\cdot}\dot{E}_{PV}$	MW
Storage capacity t_{dch}	7 –13	hours
Air Storage capacity	$(4.8\ -8.9) \bullet 10^4$	m^3
Air storage pressure range	46 –75	bar
HP H_2 Storage capacity	$(1.5\ -2.8) \bullet 10^3$	m^3
HP H_2 storage pressure range	46 –75	bar
LP H_2 Storage capacity	$(6.4\ -1.2) \bullet 10^3$	m^3
LP H_2 storage pressure range	16 –30	bar

simulations are carried out for an overall typical year, wherein power flows are calculated with a time step of 1 h in order to meet the needs of a real electrical grid.

2.2.1. Photovoltaic plant

The PV power production is calculated [12] using Eq.(1):

$$\dot{E}_{PV} = n_{PV} \bullet S_{PV} \bullet GI \bullet f_{PV} \bullet \eta_{INV} \bullet \eta_{PV} \tag{1}$$

where n_{PV} is the number of PV modules, S_{PV} the module surface, *GI* the Global Solar Irradiation, f_{PV} the derating factor for secondary losses, η_{INV} the inverter efficiency (as represented in Fig. 6 [31]) and η_{PV} the module conversion efficiency. The module conversion efficiency and the cell temperature are calculated according to Duffie et al. [32]:

$$\eta_{PV} = \eta_{PV,STC} \bullet [1 + \theta \bullet (T_{CELL} - T_{STC})] \tag{2}$$

$$T_{CELL} = max\left(T_{AMB}; \frac{T_{AMB} + (NOCT - T_{AMB,NOCT}) \bullet \frac{GI}{GI_{NOCT}} \bullet \frac{(1-\eta_{PV,STC} \bullet (1-\theta \bullet T_{STC}))}{\tau_\alpha}}{1 + (NOCT - T_{AMB,NOCT}) \bullet \frac{GI}{GI_{NOCT}} \bullet \frac{\theta \bullet \eta_{PV,STC}}{\tau_\alpha}}\right) \tag{3}$$

Hourly weather data are obtained by Meteonorm software version 7.2 [33] and refer to a site located in California. The main data and assumptions of the PV system are reported in Table 1.

2.2.2. Electrolyzer

The mathematical model for the PEM electrolyser is developed based on the work by Zhao et al. [35]. It is a steady-state model, used to

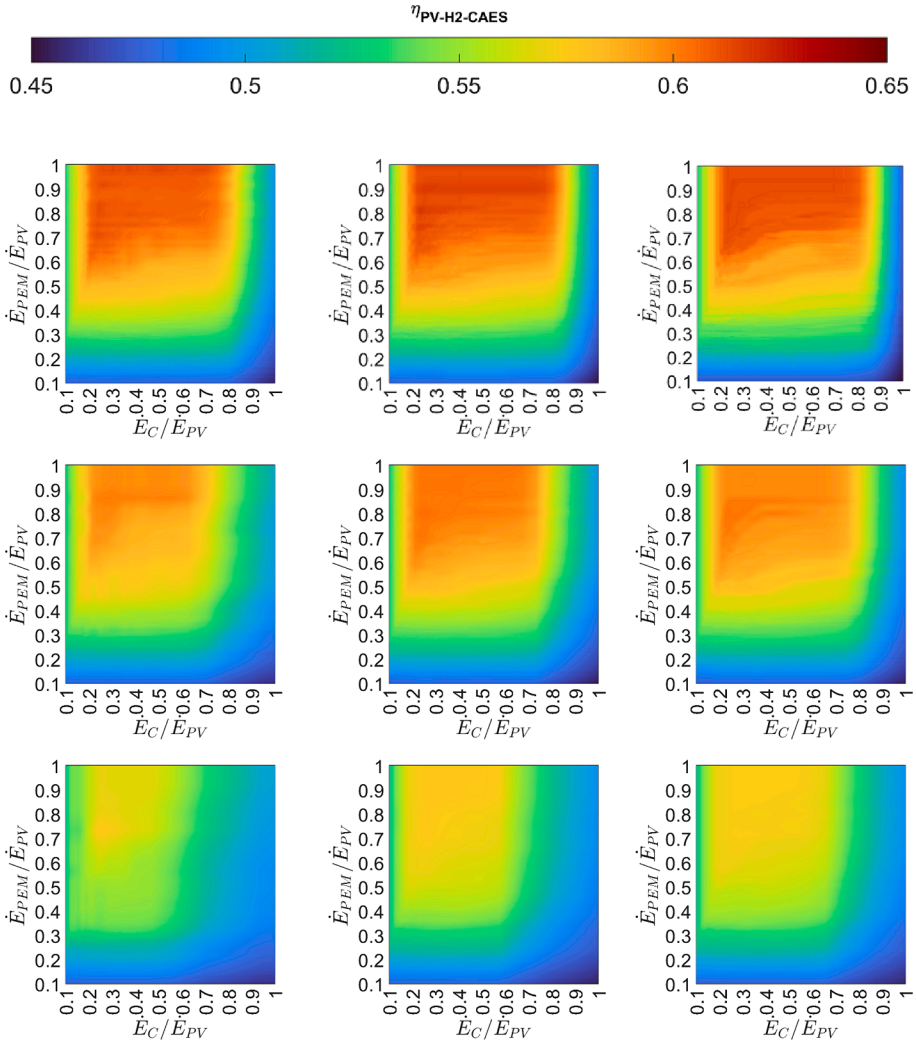

Fig. 9. η_{PV-H_2-CAES} as a function of the PV-H_2-CAES design parameters.

calculate the performance of the electrolyser considering the various losses. The cell voltage V_{cell} is calculated as:

$$V_{cell} = E + \eta_{act} + \eta_{ohm} + \eta_{diff} \tag{4}$$

where E is the open circuit voltage, η_{act} is the activation overpotential, η_{ohm} is the ohmic overpotential, and η_{diff} is the diffusion overpotential. The open circuit voltage is calculated from the Nerst equation:

$$E = E^0_{rev} + \frac{RT}{zF}\ln\left(\frac{P_{H_2}P^{\frac{1}{2}}_{O_2}}{P_{H_2O}}\right) \tag{5}$$

where E^0_{rev} is the reversible cell voltage, R is the gas constant, T is the temperature, z is the number of electrons, F is Faraday constant, and P_{H_2}, P_{H_2O} and P_{O_2} are the partial pressures of hydrogen, water, and oxygen, respectively.

The three overpotentials are calculated with the following equations:

$$\eta_{act} = \frac{RT}{\alpha_{PEM}zF} ln\left(\frac{i}{i_0}\right) \tag{6}$$

$$\eta_{diff} = \frac{RT}{\beta_{PEM}zF} ln\left(1 + \frac{i}{i_{lim}}\right) \tag{7}$$

$$\eta_{ohm} = \frac{\delta_m I}{A\sigma_m} \tag{8}$$

where α is the transfer coefficient, i_0 is the exchange current density, β is the constant coefficient, i_{lim} is the diffusion limit current density, δ_m is the thickness of the membrane and A is the membrane cross section area.

The conductivity of the proton exchange membrane σ_m is calculated with Eq. (9):

$$\sigma_m = (0.005139\lambda_E - 0.00326)\exp\left[1268\left(\frac{1}{303} - \frac{1}{T}\right)\right] \tag{9}$$

where λ_E is the humidification factor.

Finally, the hydrogen production is calculated with the Faraday Law:

$$n_{H_2} = \frac{I}{2F} \tag{10}$$

where I is the operating current, calculated based on the input power of the considered electrolyzer [36]. The PEM design parameters assumed in this study are summarized in Table 2.

Compression train

The power required by each compressor is calculated as:

$$\dot{E}_{C,i} = \dot{m}_{ch,i}\frac{\gamma_i}{\gamma_i - 1}R_i T_{i,in}\left(\beta_{C,i}^{\frac{\gamma_i - 1}{\gamma_i \eta_{C,i}}} - 1\right) \tag{11}$$

where $\dot{m}_{ch}$ is the mass flow rate of the compressor during the charge phase, γ is the specific heat ratio, R is the gas coefficient of air, T_{in} is the temperature at the inlet side of the compressor, β_C is the pressure ratio of

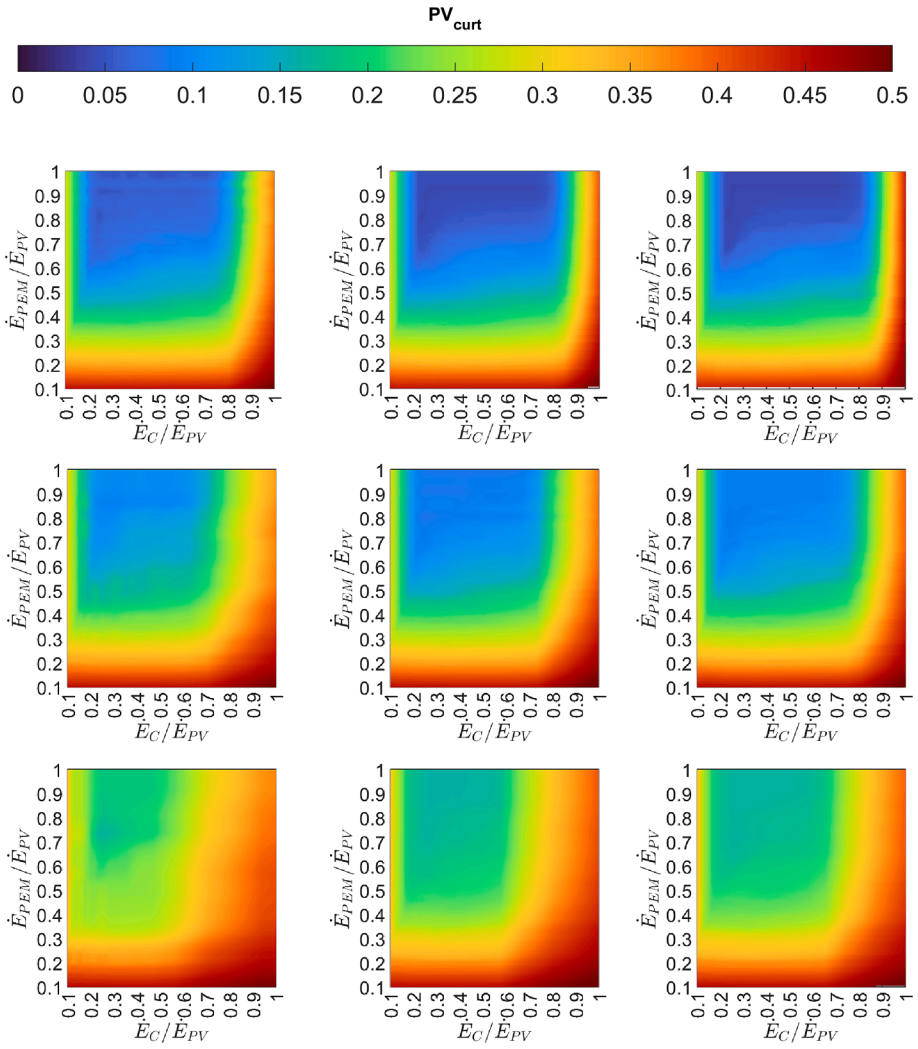

Fig. 10. PV_{curt} as a function of the PV-H_2-CAES design parameters.

the compressor, and η_c is the polytropic efficiency and the subscript i indicates either air or hydrogen. During charging, the pressure ratio increases accordingly to the pressure inside the respective storage tank. Consequently, the input power of the compressors increases.

The air compressor train comprises four multistage centrifugal compressors. The choice of centrifugal compressors is made according to Baljé [37] because of the low mass flow rate and the high-pressure ratio. The mathematical model is developed based on the Casey-Robinson method [38], used to estimate the design and off-design performance of compressors. At the outlet side of each compressor, an aftercooler is used to reduce the temperature of the compressed air, thus lowering the total power required by the compression train. Fig. 7 shows the generalized efficiency profile of the compressor in function of the generalized pressure ratio. The compressor is designed for a maximum pressure of 70 bar. It can be observed that, at low pressure ratios, the efficiency is significantly lower compared to the design point. Instead, for a generalized pressure ratio higher than 0.7, the efficiency is more than 90 % of the design efficiency.

Expansion train

The expansion train includes two turbines, two combustion chambers and a regenerator. According to Skabelund et al. [39], the system is assumed to operate in steady-state condition and with constant isentropic efficiencies for the turbines. Furthermore, except for the combustion chambers, all components are modeled without thermal and pressure losses.

The mass flow rate at the inlet of each turbine $\dot{m}_T$ is the sum of the mass flow rates of air $\dot{m}_{air}$ and fuel $\dot{m}_{fuel}$ and depends on the air–fuel ratio, which is calculated by solving the CC energy balance equation:

$$\alpha_{CC} = \frac{\dot{m}_{air}}{\dot{m}_{fuel}} = \frac{(LHV + h_{H2}) \bullet \eta_{CC} - h_g}{h_g - h_{air}} \tag{12}$$

where α_{CC} is the air–fuel ratio, LHV is the lower heating value of the fuel, and h_{H2}, h_{air} and h_g are the enthalpies of hydrogen, of the air and of the exhaust gas, respectively.

The power of each turbine is calculated by the following equation:

$$\dot{E}_t = \dot{m}_{dch} \frac{\gamma_g}{\gamma_g - 1} R_g T_{in} \left(1 - \beta_t^{\frac{\gamma_g - 1}{\gamma_g} \eta_t} \right) \tag{13}$$

In order to operate the expansion train in constant pressure mode [29] as for the McIntosh CAES plant, pressure regulators (PR) are modeled as adiabatic processes [40]:

$$T_{12} = T_{11} \bullet \left(\frac{p_{12}}{p_{11}} \right)^{\frac{\gamma - 1}{\gamma}} \tag{14}$$

The heat exchanger before the PR prevents the air stream temperature from dropping below the freezing point.

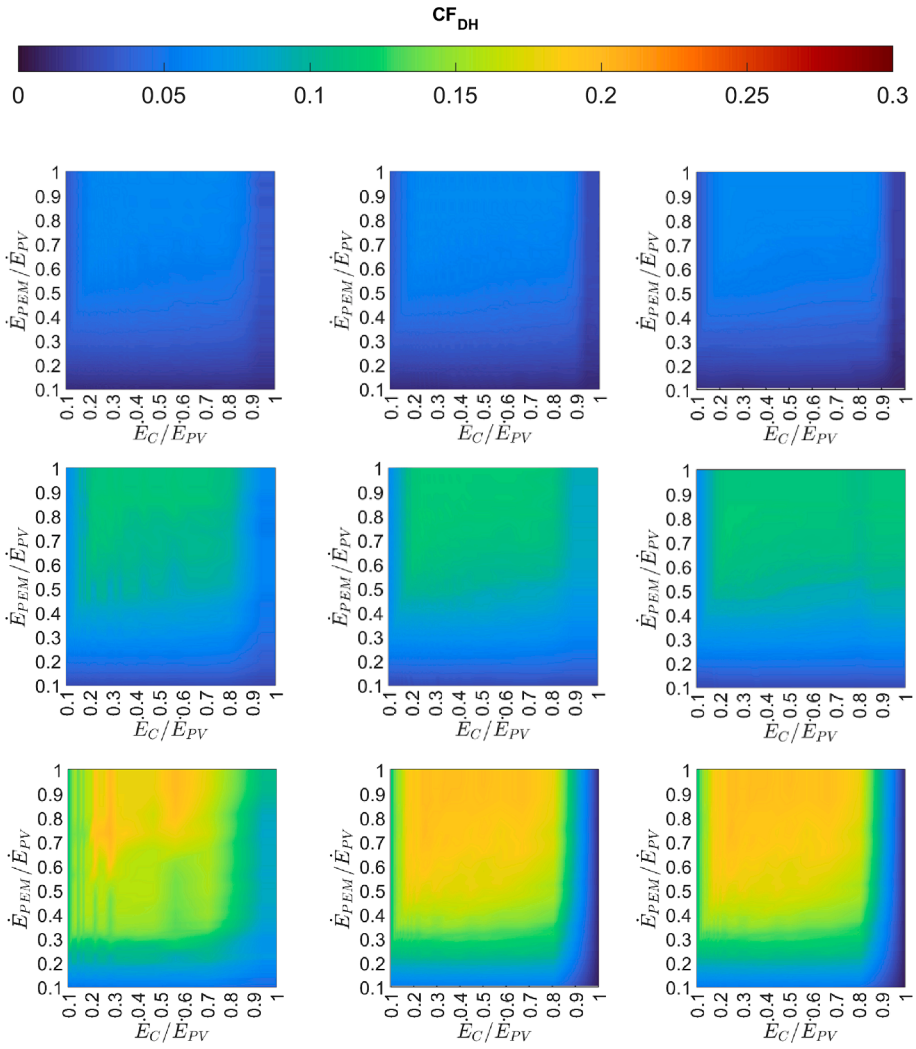

Fig. 11. CF_{DH} as a function of the PV-H_2-CAES design parameters.

2.2.3. Storage

For given values of both the rated power of the compression train and the turbines, the charge time and the discharge time strictly depend on the air and hydrogen storage capacities. The air storage volume and the hydrogen storage volume are calculated by starting from the required nominal flow rate of air and fuel [40].

The following system of equations is solved to determine the total storage volume and the mass stored at minimum pressure for both the air and hydrogen storage systems.

$$\begin{cases} p_{min,i} V_{tot,i} = m_{min,i} R_i T_{st,i} \\ p_{max,i} V_{tot,i} = \left(m_{min,i} + \dot{m}_i t_c \right) R_i T_{st,i} \end{cases} \tag{15}$$

where p_{min} is the minimum storage pressure, V_{tot} is the total storage volume, m_i is the mass stored, R_i is the gas coefficient, T_{st} is the storage temperature, p_{max} is the maximum storage pressure, $\dot{m}_i$ is the charge mass flow rate, and t_c is the charge time and the suffix i stands for either air or hydrogen. The minimum pressure for the air storage volume is determined by the operating range of the air compressors. The minimum pressure for each of the hydrogen storage tanks is instead assumed according to the operating pressure of the combustion chambers.

2.2.4. Performance indicators

The performance of the integrated PV-H_2-CAES system is evaluated by means of the three performance indicators described in the present section, which are defined with reference to the main energy flows already shown in Fig. 2. The performance indicators measure the system efficiency, the system capacity to minimize PV curtailment, and the capacity factor of the plant during dark hours.

The system efficiency (η_{PV-H_2-CAES}) measures the overall efficiency of the integrated system in delivering PV energy to the grid, either directly or through the CAES process:

$$\eta_{PV-H_2-CAES} = \frac{E_{PV,G} + E_{T,G}}{E_{PV}} \tag{16}$$

where $E_{PV,G}$ represents the energy directly fed in the grid, $E_{T,G}$ the energy generated during the CAES discharge phase and E_{PV} the PV potential energy production.

The curtailment of PV energy (PV_{CURT}) quantifies the ratio of PV energy that is curtailed due to reaching of the maximum storage capacity and the impossibility of further dispatch (neither stored nor directly fed into the grid) over the potential energy production of the PV system:

$$PV_{CURT} = \frac{E_{PV,CURT}}{E_{PV}} \tag{17}$$

The capacity factor during dark hours (CF_{DH}) is an evolution of the traditional capacity factor and measures the number of CAES equivalent generation hours over the total dark hours:

Table 4
Design parameters for maximizing the PV-H_2-CAES performance.

Parameter			
$\dot{E}_{PV}$(MW)	$\frac{1}{2}\dot{E}_T$ (21)	$1\dot{E}_T$(42)	$2\dot{E}_T$(84)
t_{dch}(h)	9	10	7
$\dot{E}_{PEM}$(MW)	0.80 $\dot{E}_{PV}$ (16.8)	0.81 $\dot{E}_{PV}$ (34.0)	0.73 $\dot{E}_{PV}$ (61.3)
$\dot{E}_C$(MW)	0.24 $\dot{E}_{PV}$ (5.0)	0.24 $\dot{E}_{PV}$ (10.1)	0.28 $\dot{E}_{PV}$ (23.5)
η_{PV-H_2-CAES} (-)	0.619	0.606	0.581
PV_{CURT}(-)	0.035	0.075	0.148
CF_{DH}(-)	0.064	0.119	0.202
H_2-CAES round-trip efficiency η_{RT}* (-)	0.345	0.345	0.345
Air storage volume (m^3)	$6.2 \bullet 10^4$	$6.9 \bullet 10^4$	$4.8 \bullet 10^4$
HP H_2 storage volume (m^3)	$1.9 \bullet 10^3$	$2.1 \bullet 10^3$	$1.5 \bullet 10^3$
LP H_2 storage volume (m^3)	$8.2 \bullet 10^2$	$9.2 \bullet 10^3$	$6.4 \bullet 10^3$
E_{PV}(GWh/y)	55.08	158.63	220.41
$E_{PV,G}$(GWh/y)	24.20	96.86	96.86
$E_{PV,CURT}$(GWh/y)	2.18	8.30	32.53
$E_{PV,H2-CAES}$(GWh/y)	28.70	53.47	91.02
$E_{PV,PEM}$(GWh/y)	20.93	38.96	66.30
$E_{PV,C}$(GWh/y)	7.77	14.51	24.72
$E_{T,G}$(GWh/y)	9.87	18.37	31.29
E_G(GWh/y)	34.07	115.23	128.16

*$\eta_{RT} = \frac{E_{T,G}}{E_{PV,H_2-CAES}}$.

$$CF_{DH} = \frac{\dot{E}_{T,G} \bullet EOH_T}{\dot{E}_{T,G} \bullet DH} = \frac{EOH_T}{DH} \quad (18)$$

where EOH_T represents the Equivalent Operating Hours of the CAES section (during discharge) and DH is the number of dark hours over a given period. CF_{DH} can also be intended as a flexibility indicator which assesses the capacity of the system to assist the grid through feed-ins of inertial energy from RES during periods of PV absence.

2.2.5. Model validation

The thermodynamic properties of different streams in the CAES cycle, calculated using the thermophysical property library CoolProp [41] are reported in Table S1 of the Supplementary Material together with the temperature-entropy diagram of the cycle (Figure S1).

Since the design parameters of the McIntosh plant are the only available data in literature, the mathematical model is validated for the un-scaled base configuration, using parameters within the range of those stated by [13,15,42,43]. Validation results are reported in Table S2 of the Supplementary Material: minimal differences are found between the present work and the reference results, attributable to the assumptions that had to be made on data not found in the literature.

3. Results and discussion

The present study assesses the performance of the PV-H_2-CAES system in the real grid scenario represented by the 2022 CAISO conditions, in relation to which specific dispatchability issues have been highlighted in the preceding sections. Apart from California, such RES-saturated power grids are already present in some parts of the world and will be so in an increasing number of locations in the near future. For this reason, the results presented in this section, along with the performance indicators introduced in Section 2.3, provide insights into the performance of this type of facilities in the electrical networks of the near future.

The present section is organized as follows: Section 3.1 presents the results of a sensitivity analysis aimed at identifying system configurations that maximize the performance of the PV-H_2-CAES system on a yearly basis, while Section 3.2 discusses one of these configurations, analyzing the seasonal trends of the performance indicators.

The sensitivity analysis is carried out by varying four design parameters: the rated power of the PV plant, the rated power of the compressor train, the rated power of the electrolyzer, and the storage

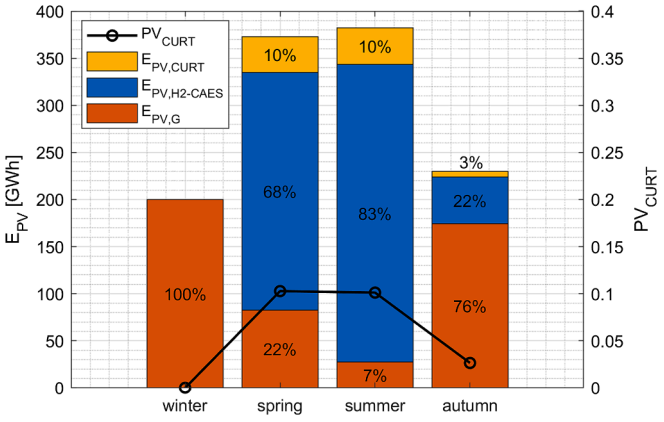

Fig. 13. Seasonal E_{PV} ($E_{PV,CAES}$, $E_{PV,G}$, $E_{PV,CURT}$) and PV_{CURT} for the set of design parameters which maximizes the performance when $\dot{E}_{PV} = \dot{E}_T$.

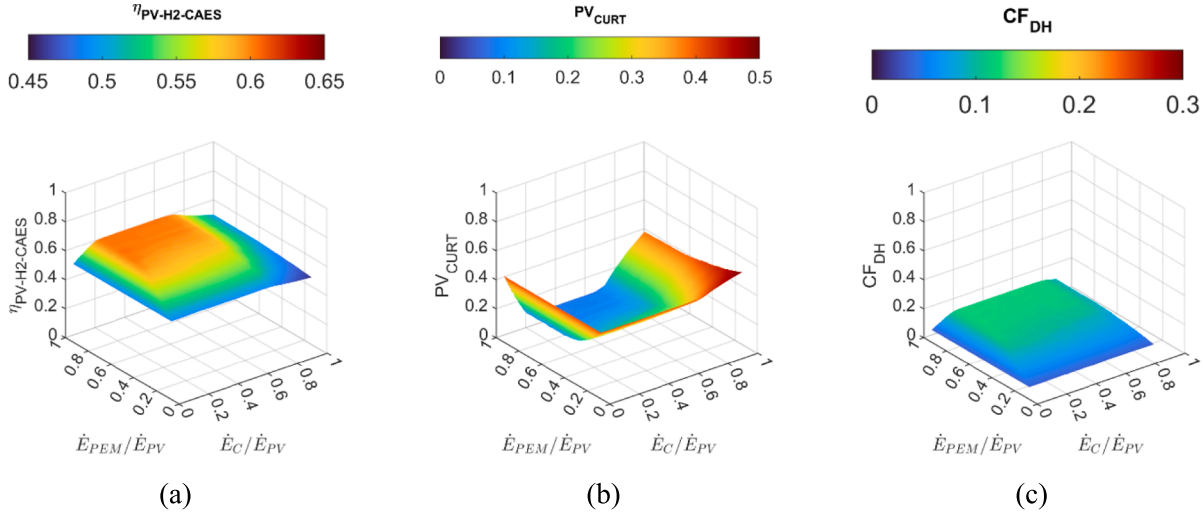

Fig. 12. Performance indicators η_{PV-H_2-CAES} (a), PV_{CURT} (b) and CF_{DH}(c) for $\dot{E}_{PV} = \dot{E}_T$.

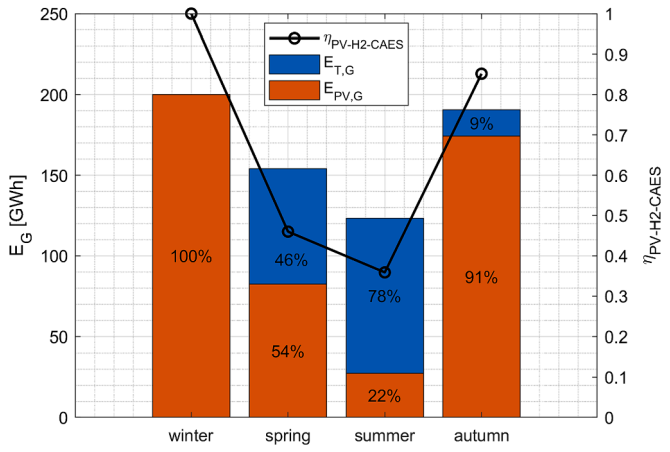

Fig. 14. Seasonal E_G ($E_{T,G}$, $E_{PV,G}$) and η_{PV-H_2-CAES} for the set of design parameters which maximizes the performance when $\dot{E}_{PV} = \dot{E}_T$.

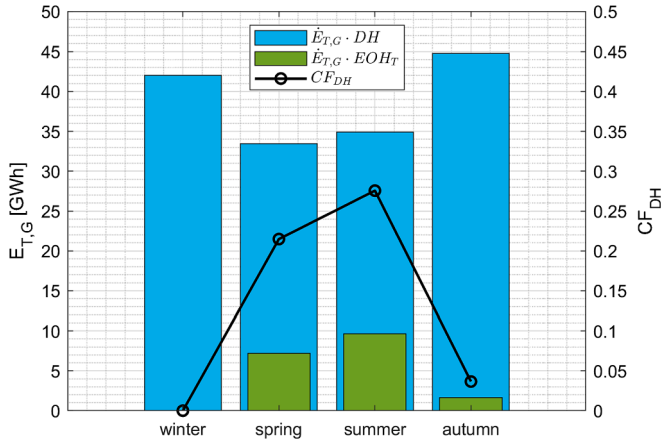

Fig. 15. Seasonal $E_{T,G}$ ($\dot{E}_{T,G} \bullet EOH_T$, $\dot{E}_{T,G} \bullet DH$) and CF_{DH} for the set of design parameters which maximizes the performance when $\dot{E}_{PV} = \dot{E}_T$.

capacity. The rated power of the PV plant ($\dot{E}_{PV}$) ranges between 0.5 and 2 times the turbine power ($\dot{E}_T$), while, considering that the compressor and the electrolyzer are powered by the PV system, their sizes ($\dot{E}_C$ and $\dot{E}_{PEM}$) vary independently in a range between 0.1 and 1 time the size of the PV plant. The storage capacity, expressed in terms of the nominal discharge duration of the CAES system at full power, is considered within the range of 7–13 h: this range is determined considering the cumulative frequency of consecutive dark hours[2] that occurred in California in 2022 and reported in Fig. 8. By the latter, it can be observed that a storage capacity of 13 h is potentially sufficient to cover nearly all (99.5 %) of the consecutive dark hours of the year. The lower storage capacity (7 h) is instead chosen as the nearest integer to the cumulative frequency value at about 20 %.

The main design parameters of the integrated PV-H_2-CAES plant are summarized in the following Table 3.

3.1. Yearly system performance

The results of the sensitivity analysis, which is conducted to determine the configuration that maximizes the system performance on a yearly base, are presented in this section. The maximum system performance is identified for highest values of η_{PV-H_2-CAES} and CF_{DH} and lowest values of PV_{CURT}.

3.1.1. System efficiency

Fig. 9 shows the variations of η_{PV-H_2-CAES} across the four design parameters ($\dot{E}_{PV}$, $\dot{E}_C$, $\dot{E}_{PEM}$, t_{dch}). Each subplot displays the system efficiency while considering variations in the compression train and the electrolyzer powers for a given value of $\dot{E}_{PV}$ and t_{dch}. The analysis is carried out over a wide range of PV power and storage capacity values, and the results are presented for three values of $\dot{E}_{PV}/\dot{E}_T$ and three values of t_{dch}.

For the design parameters here considered, the system efficiency is always included in the range of 0.45 − 0.62. Independently of $\dot{E}_{PV}$ and t_{dch}, the highest η_{PV-H_2-CAES} values are observed for $\dot{E}_{PEM}/\dot{E}_{PV}$ within the range of 0.7 − 0.9 and for $\dot{E}_C/\dot{E}_{PV}$ within the range of 0.20 − 0.25. Clearly, solutions minimizing the sizes of the electrolyzer and of the compressor train are preferable when efficiencies are equivalent. Lower $\dot{E}_{PV}/\dot{E}_T$ values lead to higher efficiencies at the expense of lower capacity factors, as reported in the following subsections.

For a given storage capacity (t_{dch}), high PV power values lead to lower system efficiencies. In fact, high amounts of PV generation are lost due to limitations in dispatchability and CAES storage capacity. As a result, the share of curtailed energy increases and, consequently, the system efficiency decreases. It should be noted that the inclusion within the system efficiency of PV losses from curtailment of RES overgeneration, in addition to PV losses due to insufficient storage capacity, is one of the novel aspects of this study.

Focusing on the area with the highest system efficiencies (orange/red coloured areas), for a given $\dot{E}_{PV}/\dot{E}_T$, increasing t_{dch} from 7 h to 10 h results in a system efficiency increment, but no further relevant improvements are observed for greater storage capacities. This implies that a 10-hour storage capacity is adequate to maximize the PV energy shift towards dark hours. In a perspective that combines economic and technical aspects, a smaller storage capacity under comparable conditions is certainly preferable.

Finally, all the graphs of Fig. 9 clearly show the influence of $\dot{E}_{PEM}/\dot{E}_{PV}$ and $\dot{E}_C/\dot{E}_{PV}$ on the system efficiency. In particular, increasing the power of the PEM electrolyzer improves the system efficiency up to a plateau, while growth of the compression train power results in raising the system efficiency up to a maximum before declining. In fact, while the electrolyzer is a modular system with a broad power range, capable of managing a wide range of fluctuating power inputs, the compressor operating power range is limited, and it is related to the air cavern pressure at any given time. As a result, not enough power is averagely provided by the PV plant for excessively large-sized compression trains, resulting in the curtailment of an increasing share of the PV power. Essentially, for compressor sizes significantly larger than the PV size, it would be necessary to substantially increase the size of the PEM electrolyzer to achieve results similar to those obtained with much smaller compressor and electrolyzer sizes.

3.1.2. Photovoltaic curtailment

Fig. 10 shows the variations of PV_{CURT} across the four design parameters. The curtailment of PV energy is included in the range of 0.04 − 0.50 and increases with $\dot{E}_{PV}$. In particular, for each configuration, the minimum curtailment rises from 4 % for $\dot{E}_{PV} = 0.5\dot{E}_T$ up to 15 % for$\dot{E}_{PV} = 2\,\dot{E}_T$, with an intermediate value of 8 % for $\dot{E}_{PV} = \dot{E}_T$. Independently of $\dot{E}_{PV}$ and t_{dch}, lowest PV_{CURT} values are found within a range of $\dot{E}_{PEM}/\dot{E}_{PV}$ between 0.7 and 0.9, and for $\dot{E}_C/\dot{E}_{PV}$ between 0.20 and 0.25. As expected, these ranges are the same which leads to the highest system efficiencies.

For a given t_{dch}, increasing the power of the PV plant leads to greater curtailment values due to the growing amount of PV energy that cannot be fed into the grid and because the CAES is unable to store it. As for the

[2] nighttime hours and of hours without solar irradiance due to particularly cloudy weather.

system efficiency, for a given value of $\dot{E}_{PV}/\dot{E}_T$, storage capacities exceeding 10 h have a negligible effect on PV curtailment.

3.1.3. Capacity factor during dark hours

Figure 11 shows CF_{DH} across the four design parameters. Overall, CF_{DH} varies between 0.02 and 0.21. Maximum values of CF_{DH} are 0.06, 0.12 and 0.21 and are achieved for $\dot{E}_{PV} = 0.5\dot{E}_T$, $\dot{E}_{PV} = \dot{E}_T$ and $\dot{E}_{PV} = 2\dot{E}_T$, respectively. As observed for the other performance indicators, the highest CF_{DH} values are found for $\dot{E}_{PEM}/\dot{E}_{PV}$ within the range $0.7 - 0.9$ and for $\dot{E}_C/\dot{E}_{PV}$ within the range $0.20 - 0.25$, independently of $\dot{E}_{PV}$ and t_{dch}. For a given t_{dch}, higher PV power leads to higher capacity factors. In fact, as more energy is made available to the CAES system, the amount of energy shifted to the dark hours increases as well. Given that the turbine power is kept constant in this analysis, increasing the PV size results in an increase of the number of EOH_T and, consequently, of CF_{DH}. This means that the system is capable of producing electrical energy for 6 %, 12 %, and 21 % of the dark hours throughout the year.

Consistently with the trends described in the previous sections, for a given $\dot{E}_{PV}/\dot{E}_T$, increasing the storage capacity over 10 h does not lead to significant improvements in CF_{DH}.

The analyses of the three performance indicators reported above allows to identify a combination of design parameters ($\dot{E}_{PEM}$, $\dot{E}_C$, t_{dch}) that maximizes the overall yearly performance of the plant, for each considered $\dot{E}_{PV}$. Each combination of parameters and the relative system performance are reported in Table 4, while a 3D view of the three performance indicator values for $\dot{E}_{PV} = \dot{E}_T$ is reported in Fig. 12.

3.2. Seasonal system performance

This section investigates the seasonal performance of the PV-H_2-CAES system, considering the set of design parameters that maximizes the system performance for $\dot{E}_{PV} = \dot{E}_T$, as summarized in Table 4. The analysis is carried out with reference to the same three indicators described above (η_{PV-H_2-CAES}, PV_{CURT}, CF_{DH}), and the results are also discussed in absolute terms.

Fig. 13 shows the seasonal trend of PV_{CURT} as well as the distribution of the potential PV energy generation between the three main flows: $E_{PV,G}$, E_{PV,H_2-CAES} and $E_{PV,CURT}$. Fig. 14 displays the seasonal variations of η_{PV-H_2-CAES} as well as the distribution of the seasonal energy generation of the PV-H_2-CAES plant, highlighting the contributions from both the direct PV feed-ins and the CAES feed-ins. Fig. 15 displays the seasonal CF_{DH} of the H_2-CAES plant, along with the seasonal maximum potential and effective CAES feed-ins.

During winter, which is the season characterized by the lowest levels of solar irradiance in California, the potential of the PV system can be fully exploited: in fact, there is no curtailment, and 100 % of the PV energy is directly fed into the grid. Consequently, the η_{PV-H_2-CAES} is equal to one and the winter CF_{DH} of the plant is equal to zero. On the contrary, during seasons with high levels of solar irradiance, namely spring and summer, only a small amount of PV energy is directly fed into the grid (22 % in spring and 7 % in summer) and almost all the remaining energy, otherwise curtailed, can be stored by the CAES system. The stored energy is subsequently used to produce energy during dark hours. Indeed, the CF_{DH} during spring and summer reaches values within the range of $0.2 - 0.3$. The energy transformation processes involved in the H_2-CAES section during spring and summer determine lower η_{PV-H_2-CAES} values compared to winter, with a minimum of about 0.36.

During autumn, the behaviour of the PV-H_2-CAES system lies between the two scenarios previously described. In fact, a significant share of energy is directly fed into the grid, while the remaining is mostly stored by the CAES system, with only 3 % of generation curtailment. In scenarios with even higher RES penetration, these results suggest that such a system could be considered a viable solution also for seasonal energy storage, although this entails a significant increase in the size of the storage sections. This way, the plant could theoretically eliminate any curtailment during the seasons with overgeneration and generate inertial power even during winter.

4. Conclusions

This study assesses the annual and seasonal performance of an integrated PV-H_2-CAES system designed to operate, with zero carbon dioxide emissions, in electrical grids with high-VRES penetration and high curtailment levels.

In a case study represented by a real grid with high-variable renewables penetration and frequent dispatchability issues, the analysis demonstrates that the hydrogen-fuelled CAES system is capable of storing for a subsequent use the otherwise curtailed renewable energy, with a system efficiency of about 62 % and a capacity factor during dark hours of about 20 %, reducing curtailment to a minimum of 4 %. The system is particularly suited to exploit PV generation during spring and summer, as it can store up to 88 % of the excess generation.

In the light of the results of this study, the integrated PV-H_2-CAES system appears a promising option to allow the connection of additional RES power even in grids with high-variable renewables penetration. Additionally, the system assists in addressing high ramp rates and ramping ranges and provides inertial power during dark hours, reinforcing the grid resilience and increasing the RES share on the energy mix.

Considering the promising results of this study, the capabilities of these hydrogen-fuelled CAES system to effectively support the expected growth of renewable capacity could be further assessed through an economic analysis, useful for evaluating the profitability of VRES in scenarios where large amounts of energy cannot be dispatched because of grid safety limitations.

CRediT authorship contribution statement

Luca Migliari: Writing – review & editing, Writing – original draft, Visualization, Validation, Software, Project administration, Methodology, Investigation, Formal analysis, Data curation, Conceptualization. **Davide Micheletto:** Writing – review & editing, Writing – original draft, Visualization, Validation, Software, Methodology, Investigation, Formal analysis, Data curation, Conceptualization. **Daniele Cocco:** Writing – review & editing, Writing – original draft, Supervision, Project administration, Formal analysis, Conceptualization, Project administration, Supervision, Writing – original draft, Writing – review & editing.

Declaration of competing interest

The authors declare that they have no known competing financial interests or personal relationships that could have appeared to influence the work reported in this paper.

Data availability

Data will be made available on request.

Acknowledgements

This paper forms part of a research project funded under the National Recovery and Resilience Plan (NRRP), Mission 4 Component 2 Investment 1.3 - Call for tender No. 1561 of 11.10.2022 of Ministero dell'Università e della Ricerca (MUR); funded by the European Union – NextGenerationEU. Project code PE0000021, Concession Decree No. 1561 of 11.10.2022 adopted by Ministero dell'Università e della Ricerca (MUR), CUP F53C22000770007, according to attachment E of Decree No. 1561/2022, Project title "Network 4 Energy Sustainable Transition – NEST".

Appendix A. Supplementary data

Supplementary data to this article can be found online at https://doi.org/10.1016/j.enconman.2024.118308.

References

[1] International Energy Agency I. Renewable Energy Market Update - June 2023. 2023.
[2] California ISO - Managing Oversupply n.d. http://www.caiso.com/informed/Pages/ManagingOversupply.aspx (accessed December 11, 2023).
[3] Irena. Power system flexibility for the energy transition, Part 1: overview for policy makers. Internat. Renew. Energy Ag., Abu Dhabi 2018;2018:1–48.
[4] López Prol J, Zilberman D. No alarms and no surprises: dynamics of renewable energy curtailment in California. Energy Econ. 2023;126:106974. https://doi.org/10.1016/J.ENECO.2023.106974.
[5] Migliari L, Cocco D, Petrollese M, Cau G. Capability of a small size CSP plant to provide dispatch power. ECOS 2016 - Proceedings of the 29th International Conference on Efficiency, Cost, Optimisation, Simulation and Environmental Impact of Energy Systems. 2016.
[6] International Energy Agency. World Energy Outlook 2022. 2022.
[7] Cocco D, Migliari L, Petrollese M. A hybrid CSP-CPV system for improving the dispatchability of solar power plants. Energy Convers Manag 2016;114:312–23. https://doi.org/10.1016/j.enconman.2016.02.015.
[8] Petrollese M, Cocco D, Migliari L, Cau G. Techno-economic analysis of a hybrid CSP-CPV power plant. ECOS 2016 - Proceedings of the 29th International Conference on Efficiency, Cost, Optimisation, Simulation and Environmental Impact of Energy Systems. 2016.
[9] Zhang Y, Davis D, Brear MJ. The role of hydrogen in decarbonizing a coupled energy system. J. Clean. Prod. ;346:131082. https://doi.org/10.1016/J.JCLEPRO.2022.131082.
[10] The Role of Low-Carbon Fuels in the Clean Energy Transitions of the Power Sector. The Role of Low-Carbon Fuels in the Clean Energy Transitions of the Power Sector 2021. https://doi.org/10.1787/A92FE011-EN.
[11] Directorate-General for Energy (European Commission), ETIP SNET, Iliceto A, Samovich N, Souza e Silva N, Ilo A. Hydrogen's impact on grids - Publications Office of the EU 2023. https://doi.org/10.2833/556144.
[12] Migliari L, Petrollese M, Cau G, Cocco D. Techno-economic assessment and grid impact of thermally-integrated pumped thermal energy storage (TI-PTES) systems coupled with photovoltaic plants for small-scale applications. J Energy Storage 2024;77:109898. https://doi.org/10.1016/J.EST.2023.109898.
[13] Nakhamkin M, Andersson L, Swensen E, Howard J, Meyer R, Schainker R, et al. Aec 110 mw caes plant: status of project. J Eng Gas Turbine Power 1992;114. https://doi.org/10.1115/1.2906644.
[14] Crotogino F. Huntorf CAES: More than 20 Years of Successful Operation. 2001.
[15] Budt M, Wolf D, Span R, Yan J. A review on compressed air energy storage: basic principles, past milestones and recent developments. Appl. Energy 2016;170:250–68. https://doi.org/10.1016/J.APENERGY.2016.02.108.
[16] Cocco D, Licheri F, Micheletto D, Tola V. ACAES systems to enhance the self-consumption rate of renewable electricity in sustainable energy communities. J. Phys. Conf. Ser. 2022;2385:012025. https://doi.org/10.1088/1742-6596/2385/1/012025.
[17] Migliari L, Micheletto D, Cocco D. Performance Analysis of a Diabatic Compressed Air Energy Storage System Fueled with Green Hydrogen. Energies 2023, Vol 16, Page 7023 2023;16:7023. https://doi.org/10.3390/EN16207023.
[18] Net Zero Roadmap: A Global Pathway to Keep the 1.5 °C Goal in Reach – Analysis - IEA n.d. https://www.iea.org/reports/net-zero-roadmap-a-global-pathway-to-keep-the-15-0c-goal-in-reach?utm_content=buffer36d79&utm_medium=social&utm_source=linkedin.com&utm_campaign=buffer (accessed October 5, 2023).
[19] ETP Clean Energy Technology Guide – Data Tools - IEA n.d. https://www.iea.org/data-and-statistics/data-tools/etp-clean-energy-technology-guide (accessed December 7, 2023).
[20] Assareh E, Ghafouri A. An innovative compressed air energy storage (CAES) using hydrogen energy integrated with geothermal and solar energy technologies: a comprehensive techno-economic analysis - different climate areas- using artificial intelligent (AI). Int. J. Hydrogen Energy 2023;48:12600–21. https://doi.org/10.1016/J.IJHYDENE.2022.11.233.
[21] Xue X, Lu D, Liu Y, Chen H, Pan P, Xu G, et al. Thermodynamic and economic analysis of new compressed air energy storage system integrated with water electrolysis and H2-fueled solid oxide fuel cell. Energy 2023;263:126114. https://doi.org/10.1016/j.energy.2022.126114.
[22] Bartela Ł. A hybrid energy storage system using compressed air and hydrogen as the energy carrier. Energy 2020;196:117088. https://doi.org/10.1016/J.ENERGY.2020.117088.
[23] Alirahmi SM, Razmi AR, Arabkoohsar A. Comprehensive assessment and multi-objective optimization of a green concept based on a combination of hydrogen and compressed air energy storage (CAES) systems. Renew. Sustain. Energy Rev. 2021;142:110850. https://doi.org/10.1016/J.RSER.2021.110850.
[24] Zhao P, Xu W, Liu A, Wu W, Wang J, Wang X. Assessment the hydrogen-electric coupled energy storage system based on hydrogen-fueled CAES and power-to-gas-to-power device considering multiple time-scale effect and actual operation constraints. Int. J. Hydrogen Energy 2023;48:9198–218. https://doi.org/10.1016/j.ijhydene.2022.12.097.
[25] Cao R, Wang Y, Li W, Ni H, Duan Y. Thermodynamics analysis of a hybrid system based on a combination of hydrogen fueled compressed air energy storage system and water electrolysis hydrogen generator. Int. J. Hydrogen Energy 2023;48:24492–503. https://doi.org/10.1016/J.IJHYDENE.2023.03.310.
[26] Shiva Kumar S, Lim H. An overview of water electrolysis technologies for green hydrogen production. Energy Rep. 2022;8:13793–813. https://doi.org/10.1016/j.egyr.2022.10.127.
[27] Schmidt O, Gambhir A, Staffell I, Hawkes A, Nelson J, Few S. Future cost and performance of water electrolysis: an expert elicitation study. Int. J. Hydrogen Energy 2017;42:30470–92. https://doi.org/10.1016/j.ijhydene.2017.10.045.
[28] Report F. EPRI-DOE handbook of energy storage for Transmission & Distribution Applications. Power 2003;2.
[29] Barbour ER, Pottie DLF. Adiabatic compressed air energy storage systems. Encyclop. Energy Storage 2022;1–4(1–4):188–203. https://doi.org/10.1016/B978-0-12-819723-3.00061-5.
[30] The MathWorks Inc. (2023). MATLAB Version: (R2023a) Update 3 n.d.
[31] Petrollese M, Concas G, Lonis F, Cocco D. Techno-economic assessment of green hydrogen valley providing multiple end-users. Int. J. Hydrogen Energy 2022;47. https://doi.org/10.1016/j.ijhydene.2022.04.210.
[32] Duffie JA, Beckman WA, Worek WM. Solar Engineering of Thermal Processes, 2nd ed. J Sol Energy Eng 1994;116. https://doi.org/10.1115/1.2930068.
[33] Meteonorm. Meteonorm Features. Https://MeteonormCom/En/Meteonorm-Features 2022.
[34] SunPower®. SunPower® X-Series Solar Panels | X22-360 n.d. https://sunpower.maxeon.com/it/sites/default/files/2019-09/sunpower-maxeon-serie-x-x22-360-x21-345-commerciale.pdf (accessed September 19, 2023).
[35] Zhao L, Brouwer J, Samuelsen S. Dynamic analysis of a self-sustainable renewable hydrogen fueling station. In: ASME 2014 12th International Conference on Fuel Cell Science, Engineering and Technology, FUELCELL 2014 Collocated with the ASME 2014 8th International Conference on Energy Sustainability; 2014. https://doi.org/10.1115/FUELCELL2014-6330.
[36] ProtonOnSite. High Capacity Hydrogen Systems M Series PEM Electrolysers. 2023.
[37] Baljé OE. A study on design criteria and matching of turbomachines: Part A—Similarity relations and design criteria of turbines. J. Eng. Power 1962;84:83–102. https://doi.org/10.1115/1.3673386.
[38] Casey M, Robinson C. A method to estimate the performance map of a centrifugal compressor stage. J. Turbomach. 2012;135. https://doi.org/10.1115/1.4006590/378454.
[39] Skabelund BB, Jenkins CD, Stechel EB, Milcarek RJ. Thermodynamic and emission analysis of a hydrogen/methane fueled gas turbine. Energy Conv. Manage.: X 2023;19. https://doi.org/10.1016/j.ecmx.2023.100394.
[40] Zafer N, Luecke GR. Stability of gas pressure regulators. App. Math. Model. 2008;32:61–82. https://doi.org/10.1016/J.APM.2006.11.003.
[41] Bell IH, Wronski J, Quoilin S, Lemort V. Pure and pseudo-pure fluid thermophysical property evaluation and the open-source thermophysical property library coolprop. Ind. Eng. Chem. Res. 2014;53:2498–508. https://doi.org/10.1021/IE4033999/SUPPL_FILE/IE4033999_SI_002.ZIP.
[42] Wang J, Lu K, Ma L, Wang J, Dooner M, Miao S, et al. Overview of compressed air energy storage and technology development. Energies 2017;10. https://doi.org/10.3390/EN10070991.
[43] Venkataramani G, Parankusam P, Ramalingam V, Wang J. A review on compressed air energy storage – a pathway for smart grid and polygeneration. Renew. Sustain. Energy Rev. 2016;62:895–907. https://doi.org/10.1016/J.RSER.2016.05.002.